ACS central science

http://pubs.acs.org/journal/acscii

Research Article

A Novel Magnetic Material by Design: Observation of Yb^{3+} with Spin-1/2 in Yb_xPt_5P

Xin Gui, Tay-Rong Chang, Kaya Wei, Marcus J. Daum, David E. Graf, Ryan E. Baumbach, Martin Mourigal,* and Weiwei Xie*

Cite This: *ACS Cent. Sci.* 2020, 6, 2023−2030

Read Online

ACCESS | Metrics & More | Article Recommendations | Supporting Information

ABSTRACT: The localized f-electrons enrich the magnetic properties in rare-earth-based intermetallics. Among those, compounds with heavier 4d and 5d transition metals are even more fascinating because anomalous electronic properties may be induced by the hybridization of 4f and itinerant conduction electrons primarily from the d orbitals. Here, we describe the observation of trivalent Yb^{3+} with $S = 1/2$ at low temperatures in Yb_xPt_5P, the first of a new family of materials. Yb_xPt_5P $(0.23 \leq x \leq 0.96)$ phases were synthesized and structurally characterized. They exhibit a large homogeneity width with the Yb ratio exclusively occupying the 1a site in the anti-$CeCoIn_5$ structure. Moreover, a sudden resistivity drop could be found in Yb_xPt_5P below ∼0.6 K, which requires further investigation. First-principles electronic structure calculations substantiate the antiferromagnetic ground state and indicate that two-dimensional nesting around the Fermi level may give rise to exotic physical properties, such as superconductivity. Yb_xPt_5P appears to be a unique case among materials.

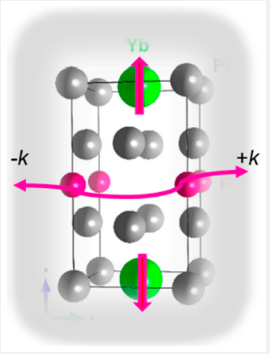

INTRODUCTION

Understanding the electronic interactions in intermetallic compounds and designing the functional materials with targeted physical properties accordingly have been long-standing challenges in materials science. On one side, the classical chemical concepts, such as charge balance arguments and electron-counting rules, do not work for intermetallic compounds with strong electron correlation, partially for the valence orbital manifold, and occasionally for relativistic effects.[1] On the other side, quantum-chemical techniques including machine learning is hindered by the limited data of materials with specific properties, such as superconductivity.[2−4] The interplay between superconductivity and magnetism, which can happen under very restricted conditions, has the potential to lead to exotic, new condensed matter physics and quantum devices. The coexistence of superconductivity and magnetism in a single material system is very rare.[5−10] Materials physicists have worked to realize this state by fabricating hybrid nanostructures that combine both superconducting and magnetic layers, and along similar lines chemists have used solvent methods to build up hybrid materials with superconducting and magnetic fragments, most of which are not fully ordered.[11−15] It is highly demanding to design and synthesize a new bulk material that displays the coexistence of superconductivity and magnetism in a single substance.

One chemical perspective for discovering new functional materials especially superconductors is to posit that similar physical properties can be observed in structural families. A well-known example is the $HoCoGa_5$-type structure motif type becoming intriguing after the discovery of heavy Fermion superconductivity in $CeCoIn_5$.[16] The indium analogues $CeTIn_5$ (T-transition metals) show an intricate interplay of superconductivity and magnetism, e.g., unconventional superconducting $CeCoIn_5$ and antiferromagnetic $CeRhIn_5$.[17]

Heavy Fermion superconductors, most of which are $4f^1$ Ce-based, are one way that the two kinds of electronic systems can interact,[16−19] and an alternative is for more weakly coupled rare earth-metal systems, such as is seen for rare earth Chevrel phases[6,20−23] and the lanthanide borocarbides.[24−28] Yb^{3+}, with a $4f^{13}$ electronic configuration, is often considered as the hole analogue of Ce^{3+}; however, only a single Yb-based heavy-Fermion superconductor, $YbAlB_4$ has been reported to date, with T_c = 0.08 K;[29] the large discrepancy must be due to unfavorable Yb-metal hybridization energies in most cases.

The ternary compound $LaPt_5As$, synthesized in rhombohedral symmetry under high pressure, provides a new avenue for research because, although nonmagnetic, it hosts superconductivity with $T_c \approx 2.6$ K.[30] Consisting of Pt-rich layered networks, superconducting $LaPt_5As$ inspired us to incorporate a magnetic rare earth element (Yb^{3+}) into the platinum-pnictide system. The much smaller ionic radius of Yb compared to La led us to replace As^{3-} with smaller P^{3-} to

Received: May 28, 2020
Published: July 1, 2020

https://dx.doi.org/10.1021/acscentsci.0c00691
ACS Cent. Sci. 2020, 6, 2023−2030

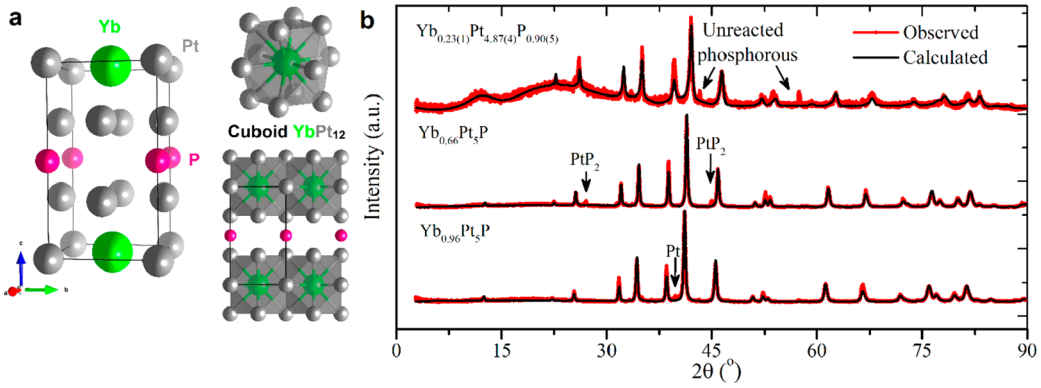

Figure 1. Structural determination and phase characterization of Yb_xPt_5P. (a) The crystal structure of $YbPt_5P$, where green, gray, and red spheres represent Yb, Pt, and P atoms, respectively. (b) The Rietveld refinements of powder X-ray diffraction patterns of Yb_xPt_5P with x = 0.25, 0.67, and 1. The red line and dot indicate the observed reflection patterns, and the black line represents the calculated pattern obtained from single crystal XRD. The calculated patterns and the peak positions of $YbPt_5P$ are indicated by green vertical ticks.

Table 1. Compositions, Phase Analyses, Lattice Constants, and Refined Compositions for Yb_xPt_5P phases[a]

			composition	
atomic % Yb loaded	impurities (manual)	phase (PXRD)	(PXRD)	(SCXRD)[b]
40	unreacted P; Pt	151-type; Pt; P	$Yb_{0.23}Pt_5P_{0.90}$	$Yb_{0.23(1)}Pt_{4.87(4)}P_{0.90(5)}$
80	Pt; PtP_2	151-type; Pt; PtP_2	$Yb_{0.67}Pt_5P$	$Yb_{0.660(4)}Pt_5P$
110	Pt	151-type	$Yb_{0.96}Pt_5P$	$Yb_{0.96(1)}Pt_5P$

[a]PXRD = powder X-ray diffraction; SCXRD = single crystal X-ray diffraction. [b]296 K; Numbers in parentheses are standard uncertainties.

stabilize a hypothetical $YbPt_5P$ at ambient pressure. This may yield both superconducting and magnetic properties in a single material.

Thus, here we report a new material Yb_xPt_5P with a thorough crystallographic and physical properties characterization. Yb_xPt_5P crystallizes in tetragonal $TlPt_5As$-type structure with the space group $P4/mmm$. The structure can be considered as the antiformat of $CeCoIn_5$. According to single-crystal X-ray diffraction, the Yb content (x) in Yb_xPt_5P varies significantly from x = 0.23−0.96. We studied the magnetic and electronic properties on two samples with x = 0.23 (1) and 0.96 (1). In both samples, we observed antiferromagnetic transitions of Yb^{3+} around 0.3 K. Moreover, zero-resistivity transition was observed around ∼0.6 K only in low ratio Yb samples, $Yb_{0.23(1)}Pt_{4.87(4)}P_{0.90(5)}$ and $Yb_{0.29(1)}Pt_5P$, but not in $Yb_{0.96(1)}Pt_5P$. Our new quantum material is a new ideal platform to study the interplay between superconductivity and magnetism. Our new quantum material appears to be a distinct platform for studying the interactions between superconductivity and magnetism, in a material where the strong spin−orbit coupling is present.

RESULTS AND DISCUSSION

Phase Information, Crystal Structure, and Chemical Composition Determination. Single-crystal X-ray diffraction (SXRD) analysis shows that Yb_xPt_5P adopts the tetragonal structure illustrated in Figure 1a, with space group $P4/mmm$, which can be considered an anti-$CeCoIn_5$-type,[12] while in Yb_xPt_5P, Yb and Pt atoms are located on the 1a and 1c sites, and in $CeCoIn_5$, the Ce and Co atoms occupy the 1c and 1a sites. The structure of Yb_xPt_5P is layered, with planes of phosphorus atoms separating square-lattice layers of truncated $YbPt_{12}$ cuboids. These cuboids host two distinct Yb−Pt distances (i.e. Yb-Pt1: 2.876 (1) Å and Yb-Pt2: 2.810 (2) Å in $Yb_{0.96(1)}Pt_5P$). The refined crystallographic data including atomic positions, site occupancies, and isotropic thermal displacements for the different Yb concentrations studied in detail are summarized in Tables S1 and S2 of the Supporting Information. Our synthetic approach yielded Yb_xPt_5P with various Yb ratios. By decreasing the occupancies of Yb on the 1a site to ∼23%, vacancies of P/Pt on 1b/4i sites appear. This aspect of the structural chemistry influences the bulk physical properties. Table 1 summarizes the synthetic results from the powder X-ray diffraction patterns and single-crystal X-ray diffraction of selected samples. Of these, the low-Yb loadings yielded a mixture of 151-phase and unreacted Pt phase, which can be distinguished by the optical microscope. Attempts to stabilize the 151-phase with homogeneous Yb occupancy by extending the annealing time results in the decomposition of 151-type phases. The powder X-ray diffraction patterns of Yb_xPt_5P are shown in Figure 1b. It can be found that Yb_xPt_5P phases were obtained with slight Pt or PtP_2 impurities with a different occupancy of Yb. The samples used to perform the physical properties measurements were taken from the same specimen. After measurements were done, the samples were ground into powder, and the powder X-ray diffraction measurement confirmed the chemical compositions again.

For the X-ray powder diffraction patterns, all scale factors and lattice parameters were refined, while the displacement parameters of all atoms were assumed to be anisotropic. The refined lattice parameters for Yb_xPt_5P phases showed a 1.54% and 2.64% increase along a and c according to powder X-ray diffraction as the Yb ratio increased from 25 to 100 atomic percent. Single crystals showed a similar trend. Analysis of samples all fall within various ratios of Yb in the phase. Does Yb still show a 3+ oxidation state in the intermetallic Yb_xPt_5P? With the question in mind, X-ray photoelectron spectroscopy (XPS) experiments were performed on $Yb_{0.660(4)}Pt_5P$ and $Yb_{0.96(1)}Pt_5P$, which confirmed the 3+ oxidation state of Yb in both samples, as shown in Figure S2.

https://dx.doi.org/10.1021/acscentsci.0c00691
ACS Cent. Sci. 2020, 6, 2023−2030

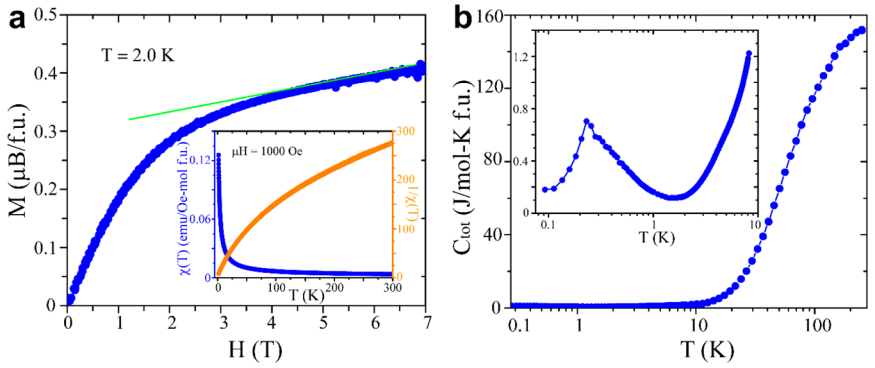

Figure 2. Antiferromagnetism in $Yb_{0.23(1)}Pt_{4.87(4)}P_{0.90(5)}$. (a) (Main panel) Isothermal magnetization up to 7 T at 2.0 K for $Yb_{0.23(1)}Pt_{4.87(4)}P_{0.90(5)}$. (Inset) The temperature-dependence of the magnetic susceptibility for $Yb_{0.23(1)}Pt_{4.87(4)}P_{0.90(5)}$ from 1.8 to 300 K measured under an applied field of 1000 Oe, data as indicated by the blue line for magnetic susceptibility and orange line for the inverse magnetic susceptibility. Green lines show the Curie−Weiss fitting of the inverse χ data at high temperature. (b) (Main panel) Heat capacity measurements for $Yb_{0.23(1)}Pt_{4.87(4)}P_{0.90(5)}$ from 0.1 to 150 K. (Inset) C_{tot}/T vs T^2 for $Yb_{0.23(1)}Pt_{4.87(4)}P_{0.90(5)}$ with magnetic transition occurring at 0.23 K.

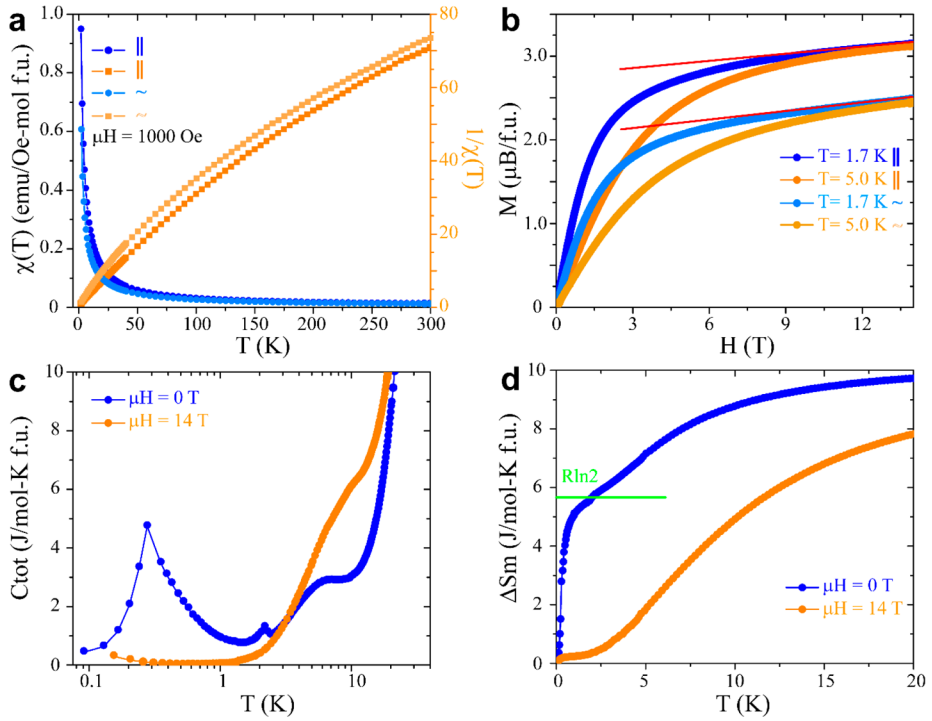

Figure 3. Antiferromagnetism in $Yb_{0.96(1)}Pt_5P$. (a) The temperature-dependence of the magnetic susceptibility for $Yb_{0.96(1)}Pt_5P$ from 1.8 to 300 K measured under an applied field of 1000 Oe, data as indicated by the blue and light blue solid circles for the field along the long axis of the piece and the field perpendicular to the long axis of the piece, respectively. Orange and brown lines show the inverse temperature-dependence of the magnetic susceptibility. Green lines show the Curie−Weiss fitting of the inverse χ data at high temperature and low temperature, respectively. (b) The magnetic behavior for $Yb_{0.96(1)}Pt_5P$ up to 14 T at 1.7 and 5 K. (c) Heat capacity measurement with/without applied magnetic field with the emphasis on the magnetic ordering transition around 0.28 K. (d) Entropy change related to the magnetic ordering of Yb^{3+} in $Yb_{0.96(1)}Pt_5P$ without an applied field.

Antiferromagnetic Ordering in Yb_xPt_5P. The magnetic susceptibility is shown as the inset of Figure 2a for a low ratio Yb sample with the chemical composition $Yb_{0.23(1)}Pt_{4.87(4)}P_{0.90(5)}$ confirmed by SEM-EDX. The data were fitted over the high-temperature region (HT from 225 to 300 K) and the low-temperature region (LT from 1.8 to 15 K) to the Curie−Weiss law without a diamagnetic correction. The effective moment of μ_{eff} = 4.21(5) μ_B/f.u. obtained for the HT range is reduced to μ_{eff} = 1.82(9) μ_B/f.u. in the LT range, where it is associated with a negative Weiss temperature θ_W = −1.97 K indicative of an antiferromagnetic tendency. The isothermal magnetization at 2K in Figure 2a (main panel) shows a negligible hysteresis and a saturation field around ∼25 kOe with a saturation magnetization around 0.3 μ_B/Yb. The heat capacity measurement, shown in Figure 2b, illustrates a clearly magnetic transition peak around 0.23 K and the large entropy change in $Yb_{0.25}Pt_5P$.

As the Yb ratio to Yb_xPt_5P increases to $Yb_{0.96(1)}Pt_5P$, the magnetic characterization of $Yb_{0.96(1)}Pt_5P$ is shown in Figure 3a,b. The inverse susceptibility does not show any linear Curie−Weiss behavior until below 30 K, indicating low-lying crystal-electric-field (CEF) levels. These CEF levels are slightly lower than in other Yb^{3+} systems in octahedral O environments. The Weiss constant is on the order of −2.2 to −2.7 K,

https://dx.doi.org/10.1021/acscentsci.0c00691
ACS Cent. Sci. 2020, 6, 2023−2030

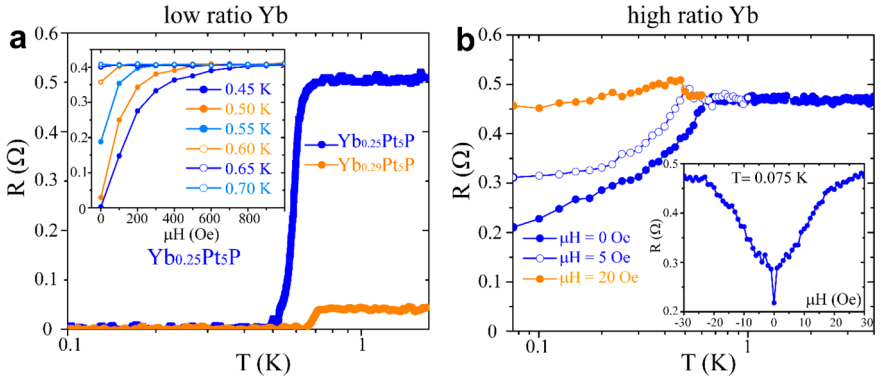

Figure 4. (a) Zero-resistance transition observed in low-Yb concentration samples for $Yb_{0.23(1)}Pt_{4.87(4)}P_{0.90(5)}$ and $Yb_{0.29(1)}Pt_5P$. (Main panel) Electrical resistivity measurements for $Yb_{0.23(1)}Pt_{4.87(4)}P_{0.90(5)}$ and $Yb_{0.29(1)}Pt_5P$ from 0.1 to 300 K. (Inset) Field-dependent resistivity of $Yb_{0.23(1)}Pt_{4.87(4)}P_{0.90(5)}$ at various temperatures (0.45, 0.50, 0.55, 0.60, 0.65, 0.7 K). (b) Failed zero-resistance transition observed in high-Yb concentration samples. (Inset) The temperature-dependent resistivity for $Yb_{0.96(1)}Pt_5P$ from 0.05 to 4 K measured under various applied fields with ADR mode conducted with 100 μA at 128 Hz.

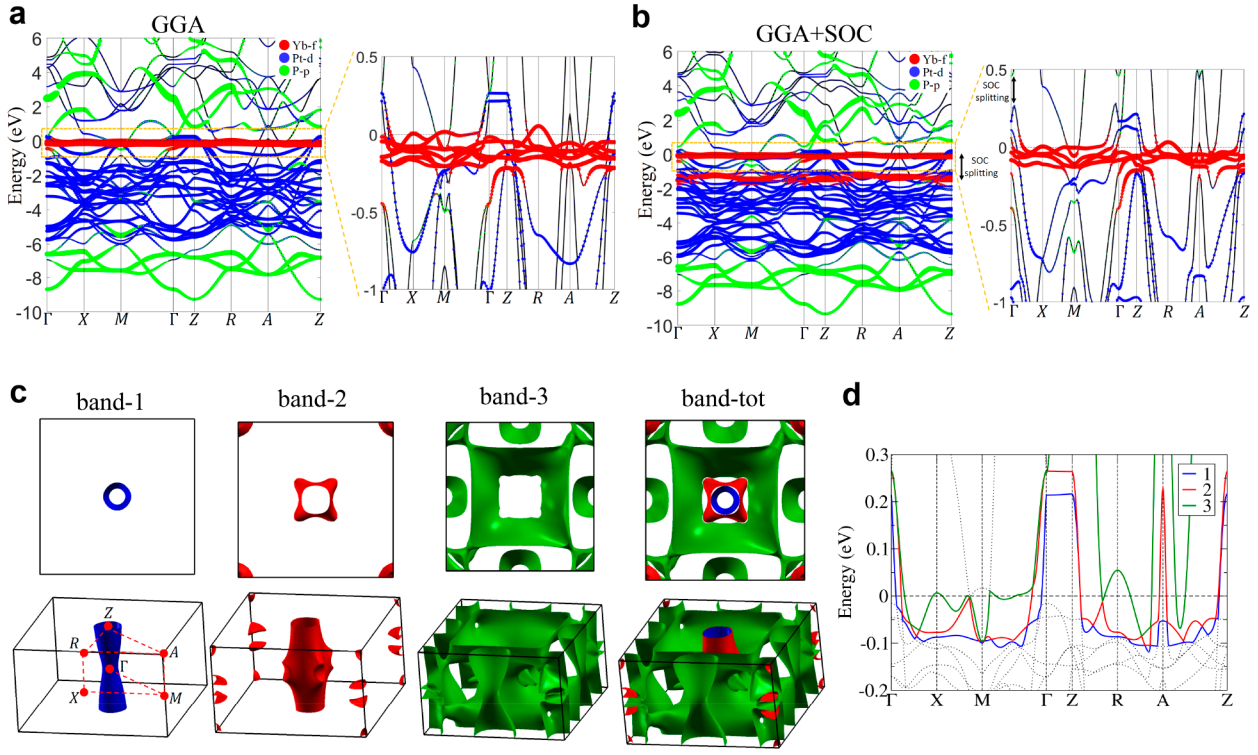

Figure 5. Calculated bulk band structure and Fermi surface of $YbPt_5P$ in its nonmagnetic phase. (a) The bulk band structure of $YbPt_5P$ based on GGA calculations without the inclusion of spin−orbit coupling. The Fermi energy is zero. The red, blue, and green dots indicate Yb-4f, Pt-5d, and P-3p orbitals, respectively. (b) Same as (a) but with the inclusion of spin−orbit coupling (SOC). The Yb-4f bands split into the j = 7/2 (around E_F) and j = 5/2 (−1.5 eV below E_F) states by SOC. (c) The bulk Fermi surface of nonmagnetic $YbPt_5P$ based on GGA calculations. The corresponding band numbers are labeled in (d). Zoom-in band structure. The bands that cross Fermi level are labeled by blue, red, and green lines, respectively.

which strongly depend on the field directions and the fitting range. This indicates there is possibly never a real Curie−Weiss regime in this sample due to CEF levels (at high T range) and strong spin−orbit interactions between spins (at low T range). The field-dependent magnetization has different orientations in the magnetic field. Orientation "||" means the field along the long axis of the piece. Orientation "~" means the field perpendicular to the long axis of the piece. The results show only a weak orientation dependence with saturated magnetization values of Ms(||) = 2.7 μ_B/f.u. and Ms (~) = 2.0 μ_B/f.u. with the effective spin-1/2 and g-tensors of 5.4 and 4 depending on the field direction. The degree of spin-space anisotropy is consistent with observation of other Yb^{3+} based insulating magnets. The normal heat capacity measurements up to 200 K in both 0 and 10 T can be fitted using a double Debye model with an extraction of a "phonon background" for the extraction of entropy. The significant shift of the magnetic specific heat capacity between 0 and 10 T is consistent with the large g-tensor. Without an applied magnetic field, in addition to the sharp peak at 0.28 K, there is a broad feature around 4 K that may be contributed from a low-lying CEF level. The magnetic entropy change (obtained after subtracting the

https://dx.doi.org/10.1021/acscentsci.0c00691
ACS Cent. Sci. 2020, 6, 2023−2030

"phonon background") indicates that there is indeed one effective $S = 1/2$ degrees of freedom per formula unit at temperatures below 3 K.

Zero-Resistance Transition Observed in $Yb_{0.25}Pt_5P$ but Suppressed in $YbPt_5P$. Figure 4a presents zero-resistance transitions of two samples with $x = 0.23$ (1) and 0.29 (1). The resistivity curve from 1.8 to 300 K is consistent with what is expected for a metal in $Yb_{0.23(1)}Pt_{4.87(4)}P_{0.90(5)}$ and $Yb_{0.29(1)}Pt_5P$ without a phase transition shown in Figure S3. The relatively small RRR may originate from defects on the Yb site. A drop to zero resistance is clearly seen at low temperatures, indicating the presence of a zero-resistance transition and highly possible a superconducting transition. The midpoints of the resistive transition of $Yb_{0.23(1)}Pt_{4.87(4)}P_{0.90(5)}$ and $Yb_{0.29(1)}Pt_5P$ are ~0.6 and 0.65 K, respectively. To further characterize the zero-resistance transition, the inset of Figure 4a shows the field-dependent resistivity curve of $Yb_{0.23(1)}Pt_{4.87(4)}P_{0.90(5)}$. After a magnetic field was applied at various temperatures, the superconducting transition was suppressed gradually, which indicates that the strong spin−orbit coupling effects on Yb and Pt have a negligible impact on the upper critical field of superconductivity. Moreover, the isostructural $Y_{0.34}Pt_5P/Y_{0.45}Pt_5P$ and Pt_5P_2 (PtP_2 is a semiconductor without resistance signal detected below 10 K) were synthesized and characterized with no superconductivity observed above 0.4 K, as shown in Figures S4 and S5, which can basically exclude the possibility that accidental impurities in Yb-based samples can contribute to the zero-resistance transition in resistivity measurements since both compounds were synthesized with an identical procedure. The heat capacity measurements for $Yb_{0.29(1)}Pt_5P$ in Figure S6 show a small kink around 0.6 K, which is consistent with the zero-resistance transition in resistivity. However, the large entropy changes from the magnetic transition of Yb^{3+} in Figure 2b make the subtle superconducting transition less possible to be observed. The similar problem occurs in the magnetic susceptibility measurements. Further study is required to confirm the superconductivity in the low ratio Yb samples. On the other side, the electric transport measurement of $Yb_{0.96(1)}Pt_5P$ shows a failed superconducting transition starting from 0.6 K illustrated in Figure 4b.

Electronic Structure and 2D Nesting in $YbPt_5P$. In order to further understand the nature of the ground state properties of $YbPt_5P$, we performed first-principles calculations on the bulk band structure based on generalized gradient approximation (GGA) and GGA with SOC (GGA+SOC) methods, as shown in Figure 5. Our GGA and GGA+SOC calculations reveal a metallic ground state. From the orbital decomposition (Figure 5a), we find the flat and narrow Yb-4f bands are located around E_F from −0.25 eV. Contrary to Yb-4f localized states, Pt-5d orbitals exhibit opposed behavior. The itinerant hole-like Pt-5d bands with a larger band dispersion span across E_F and interact with the Yb-4f localized bands near E_F, leading to a complex Fermi surface (FS). The P-3p orbitals split into two components. The upper part displays electron-like band dispersion above E_F and hybridizes strongly with Pt-5d bands, while the lower part lies about −7 eV below E_F. Figure 5c shows the three-dimensional (3D) FS of $YbPt_5P$, and the corresponding band numbers are labeled in Figure 5d. The FS of $YbPt_5P$ mainly contains four nearly 2D pockets (Figure 5c,d). Two tube-like and one bigger funnel-like hole-type pockets around point (band-1, band-2, and band-3) and another one hole-type pocket around X point (band-3). These nearly 2D FS may induce a superconducting state or an antiferromagnetic magnetic (AFM) phase in $YbPt_5P$, resulting from the FS nesting effect. It is also noted that the FS of $YbPt_5P$ is much different from the LDA band structure of heavy Fermion $CeCoIn_5$ in which there are two Fermi sheets around M point and the FS displays a much stronger k_z dispersion at point. This difference implies that the nature of the ground state of $YbPt_5P$ may be entirely distinct from the typical heavy Fermion system. By projecting the band structure onto the cubic harmonics basis, we find the FS of the occupied bands around E_F comes mainly from the Pt1-, Pt2-, and Yb-f (except Yb-) orbitals (Figure S7). The 3D real-space charge density distribution within the energy interval ($E_F \approx -10$ meV) clearly shows this orbital anisotropy feature (Figure S8). In this sense, the in-plane hopping strength is stronger than the out-of-plane one, consequently exhibiting nearly 2D FS characteristic. When SOC is turned on (Figure 5b), Yb-4f bands split into the $j = 7/2$ and $j = 5/2$ states by SOC. The $j = 7/2$ states dominate E_F while the $j = 5/2$ states are shifted to −1.5 eV below E_F. In addition, the strong SOC effect gap out the band crossing points between Pt-5d and P-3p orbitals around the point and further enhances the band splitting of the Yb-4f and Pt-5d hybridized anticrossing gap around E_F. Since the FS pattern of $YbPt_5P$ is significantly distinct from the heavy Fermion Ce-115 family, the detailed theoretical modeling and experimental tests of the effect of f−d interaction in this material are left as an open question for future studies. Finally, we consider the electronic interactions via GGA plus correlation parameter U (GGA+U) calculations. We see the Yb-4f bands drop below E_F as increasing the value of U (Figure S9). As Yb-4f bands move to higher binding energies, their hybridization with conduction bands become smaller. The Pt-5d orbitals, on the other hand, are pushed more toward E_F with increasing U and interact with P-3p states. Moreover, the SOC effect splits the Yb-4f state and further enhances the band splitting of crossing states, resulting in a continuous energy gap through the whole Brillouin zone.

CONCLUSIONS

Yb_xPt_5P ($0.23 \le x \le 0.96$) phases exhibit magnetism in all Yb concentrations and possible superconducting traces in low-Yb-ratio samples solely. The isostructural materials can be synthesized with other rare earths, with a variety of strange results expected. The coexistence of such strongly competing electronic states in a single substance itself makes this material remarkable. Moreover, the fact that the strong spin−orbit coupling of the Pt electrons must have an influence in determining the properties makes it truly novel. The complexity of the interactions between magnetism and possible superconductivity in this new materials family will push the frontiers of our knowledge of electronic and magnetic properties of materials into new areas and provide fertile ground for developing our still-emergent understanding of quantum materials.

EXPERIMENTAL SECTION

Synthesis. Yb_xPt_5P samples with several loading compositions ($x = 0.4$, 0.5, 0.8, and 1.1) were synthesized by a high-temperature solid-state method. Stoichiometric elemental Yb (<200 mesh, Alfa Aesar, ≥ 99.9%), Pt (~22 mesh, Beantown Chemical, ≥ 99.99%), and red P (~100 mesh, Beantown Chemical, ≥ 99%) were mixed well and pressed into a pellet

https://dx.doi.org/10.1021/acscentsci.0c00691
ACS Cent. Sci. 2020, 6, 2023−2030

inside an argon-filled glovebox. The pellet was placed in an alumina crucible which was then sealed in an evacuated quartz tube. Heat treatment to 950 °C was carried out at a rate of 30 °C per hour in a Thermo Scientific furnace. After being held at 950 °C for 2 days, the tubes were slowly cooled to room temperature in 5 days. On the basis of our experiments, heating at 950 °C longer than 10 days would lead to the decomposition of Yb_xPt_5P and a low ratio of Yb less than $x = 0.5$ will less possibly yield the appropriate phases. Small single crystals ($\sim 0.4 \times 0.2 \times 0.02$ mm^3) were attached to the bulk polycrystalline material, as shown in Figure S1. In most of the cases, some impurities appeared as black powder, which can be removed by soaking in ethanol in an ultrasonic bath for 20 min. Yb_xPt_5P is resistant to both air and moisture.

Phase Identification. The phase purity was determined by using a Rigaku MiniFlex 600 powder X-ray diffractometer (XRD) with Cu K_α radiation (λ = 1.5406 Å, Ge monochromator). A long scan with the Bragg angle ranging from 3° to 90° in a step of 0.005° at a rate of 0.35°/min was performed for each sample. The Rietveld method was utilized to fit the powder XRD pattern in the Fullprof Suite according to the calculated pattern from single crystal data.[31]

Structure Determination. Multiple pieces of crystals ($\sim 20 \times 40 \times 40$ μm^3) were measured to get precise structural information. A Bruker Apex II diffractometer equipped with Mo radiation ($\lambda_{K\alpha}$ = 0.71073 Å) was applied to explore the crystal structure at room temperature. The small crystals were stuck to a Kapton loop with glycerol. Four different positions were chosen to take the measurement with an exposure time of 10 s per frame and the scanning 2θ width of 0.5°. Direct methods and full-matrix least-squares on F^2 models with *SHELXTL* package were applied to solve the structure.[32] Data acquisition was obtained *via* Bruker *SMART* software with the corrections on Lorentz and polarization effect done by *SAINT* program. Numerical absorption corrections were accomplished with *XPREP*, which is based on the face-index modeling.[33]

Physical Property Measurements. All the physical property measurements were performed on pieces of as-grown samples extracted from the sample crucible. The measured pieces consisted of a mixture of polycrystalline matrix and single crystals which were semirandomly oriented with respect to each other. Magnetization measurements were carried out for temperatures T = 1.8−300 K using a vibrating sample magnetometer (VSM) in Quantum Design PPMS systems. The heat capacity was measured for T = 0.05−2 K using a dilution refrigerator (DR) and for T = 2−200 K using the heat capacity (HC) option of the same Quantum Design PPMS systems. Electrical resistivity measurements were performed in a four-wire configuration with platinum or gold wires and silver contacts for T = 0.1−300 K using the adiabatic demagnetization refrigerator (ADR) option or using the combination of dilution refrigerator and electrical transport (ETO) options.

Electronic Structure Calculation. The bulk electronic structures of $YbPt_5P$ were computed using the projector augmented wave method[34,35] as implemented in the VASP package[36] within the generalized gradient approximation (GGA)[37] and GGA plus Hubbard U (GGA+U)[38] scheme. On-site U = 7 and 4 eV were used for Yb f-orbitals and Pt d-orbitals, respectively. The spin−orbit coupling (SOC) was included self-consistently in the calculations of electronic structures with a Monkhorst−Pack k-point mesh 20 × 20 × 10. The experimental structural parameters were employed.

X-ray Photoelectron Spectroscopy (XPS). The oxidation states of Yb, Pt, and P atoms for $Yb_{0.67}Pt_5P$ and $YbPt_5P$ are determined by a Kratos AXIS 165 XPS/AES equipped with a standard Mg/Al and high-performance Al monochromatic source in an evacuated (10^{-9} Torr) chamber at room temperature.

■ ASSOCIATED CONTENT

Supporting Information

The Supporting Information is available free of charge at https://pubs.acs.org/doi/10.1021/acscentsci.0c00691.

Crystallographic data; equivalent isotropic displacement parameters; crystal picture; XPS data; resistivity from 0.1 to 300 K for $Yb_{0.23(1)}Pt_{4.87(4)}P_{0.90(5)}$ and $Yb_{0.29(1)}Pt_5P$; resistivity measurement of $Y_{0.34}Pt_5P$, $Y_{0.45}Pt_5P$, and Pt_5P_2; heat capacity measurement for $Yb_{0.29(1)}Pt_5P$ from 0.35 to 1 K; GGA bulk band structures with projection of various orbitals onto the cubic harmonics basis; 3D real-space charge density distribution; bulk band structures of GGA+U and GGA+U+SOC (PDF)

■ AUTHOR INFORMATION

Corresponding Authors

Weiwei Xie − *Department of Chemistry, Louisiana State University, Baton Rouge, Louisiana 70803, United States;* orcid.org/0000-0002-5500-8195; Email: weiweix@lsu.edu

Martin Mourigal − *School of Physics, Georgia Institute of Technology, Atlanta, Georgia 30322, United States;* Email: mourigal@gatech.edu

Authors

Xin Gui − *Department of Chemistry, Louisiana State University, Baton Rouge, Louisiana 70803, United States*

Tay-Rong Chang − *Department of Physics, National Cheng Kung University, Tainan, Taiwan 70101; Center for Quantum Frontiers of Research & Technology (QFort), Tainan, Taiwan 70101;* orcid.org/0000-0003-1222-2527

Kaya Wei − *National High Magnetic Field Laboratory, Tallahassee, Florida 32306, United States*

Marcus J. Daum − *School of Physics, Georgia Institute of Technology, Atlanta, Georgia 30322, United States*

David E. Graf − *National High Magnetic Field Laboratory, Tallahassee, Florida 32306, United States*

Ryan E. Baumbach − *National High Magnetic Field Laboratory, Tallahassee, Florida 32306, United States; Department of Physics, Florida State University, Tallahassee, Florida 32306, United States*

Complete contact information is available at: https://pubs.acs.org/10.1021/acscentsci.0c00691

Notes

The authors declare no competing financial interest.

■ ACKNOWLEDGMENTS

The work at LSU is supported by the Beckman Young Investigator (BYI) Program and NSF-DMR-1944965. The work of M.D. and M.M. at Georgia Tech was supported by the National Science Foundation through Grant NSF-DMR-1750186. T.-R.C. was supported by the Young Scholar Fellowship Program from the Ministry of Science and Technology (MOST) in Taiwan, under a MOST grant for the Columbus Program MOST108-2636- M-006-002, Na-

tional Cheng Kung University, Taiwan, and National Center for Theoretical Sciences, Taiwan. This work was supported partially by the MOST, Taiwan, Grant MOST107-2627-E-006-001. A portion of this work was performed at the National High Magnetic Field Laboratory, which is supported by the National Science Foundation Cooperative Agreement No. DMR-1644779 and the State of Florida. K.W. acknowledges the support of the Jack E. Crow Postdoctoral Fellowship. Electrical transport, magnetization, and heat capacity measurements performed by REB were supported by the Center for Actinide Science and Technology, an Energy Frontier Research Center funded by the U.S. Department of Energy (DOE), Office of Science, Basic Energy Sciences (BES), under Award No. DESC0016568.

REFERENCES

(1) Fedorchuk, A.; Grin, Y. Crystal Structure and Chemical Bonding in Gallides of Rare-Earth Metals. In *Handbook on the Physics and Chemistry of Rare Earths*; Elsevier, 2018; pp 81−143.
(2) Meredig, B.; Antono, E.; Church, C.; Hutchinson, M.; Ling, J.; Paradiso, S.; Blaiszik, B.; Foster, I.; Gibbons, B.; Hattrick-Simpers, J.; Mehta, A.; Ward, L. Can machine learning identify the next high-temperature superconductor? Examining extrapolation performance for materials discovery. *Mol. Syst. Des. Eng.* **2018**, *3*, 819−825.
(3) Hamidieh, K. A data-driven statistical model for predicting the critical temperature of a superconductor. *Comput. Mater. Sci.* **2018**, *154*, 346−354.
(4) Matsumoto, R.; Hou, Z.; Hara, H.; Adachi, S.; Takeya, H.; Irifune, T.; Terakura, K.; Takano, Y. Two pressure-induced superconducting transitions in $SnBi_2Se_4$ explored by data-driven materials search: new approach to developing novel functional materials including thermoelectric and superconducting materials. *Appl. Phys. Express* **2018**, *11*, 093101.
(5) Stewart, G. R.; Fisk, Z.; Willis, J. O.; Smith, J. L. Possibility of Coexistence of Bulk Superconductivity and Spin Fluctuations in UPt_3. In *Ten Years of Superconductivity: 1980−1990*; Ott, H. R., Ed.; Springer Netherlands, 1993; pp 85−88.
(6) Aoki, D.; Huxley, A.; Ressouche, E.; Braithwaite, D.; Flouquet, J.; Brison, J. P.; Lhotel, E.; Paulsen, C. Coexistence of superconductivity and ferromagnetism in URhGe. *Nature* **2001**, *413*, 613.
(7) Siegrist, T.; Zandbergen, H. W.; Cava, R. J.; Krajewski, J. J.; Peck, W. F. The crystal structure of supercondu cting $LuNi_2B_2C$ and the related phase LuNiBC. *Nature* **1994**, *367*, 254.
(8) Cava, R. J.; Takagi, H.; Batlogg, B.; Zandbergen, H. W.; Krajewski, J. J.; Peck, W. F., Jr; Van Dover, R. B.; Felder, R. J.; Siegrist, T.; Mizuhashi, K.; et al. Superconductivity at 23 K in yttrium palladium boride carbide. *Nature* **1994**, *367*, 146.
(9) Ott, H. R.; Fertig, W. A.; Johnston, D. C.; Maple, M. B.; Matthias, B. T. Superconducting and magnetic properties of $ErRh_4B_4$. *J. Phys. Colloques* **1978**, *39*, C6-375−C6-376.
(10) Ishikawa, M.; Fischer, Ø. Destruction of superconductivity by magnetic ordering in $Ho_{1.2}Mo_6S_8$. *Solid State Commun.* **1977**, *23*, 37−39.
(11) Goldman, A. M.; Vas'ko, V.; Kraus, P.; Nikolaev, K.; Larkin, V. A. Cuprate/Manganite heterostructures. *J. Magn. Magn. Mater.* **1999**, *200*, 69−82.
(12) Mühge, T.; Garif'yanov, N. N.; Goryunov, Y. V.; Khaliullin, G. G.; Tagirov, L. R.; Westerholt, K.; Garifullin, I. A.; Zabel, H. Possible Origin for Oscillatory Superconducting Transition Temperature in Superconductor/Ferromagnet Multilayers. *Phys. Rev. Lett.* **1996**, *77*, 1857−1860.
(13) Martin, L.; Turner, S. S.; Day, P.; Mabbs, F. E.; McInnes, E. J. L. New molecular superconductor containing paramagnetic chromium(iii)ions. *Chem. Commun.* **1997**, *15*, 1367−1368.
(14) Ojima, E.; Fujiwara, H.; Kato, K.; Kobayashi, H.; Tanaka, H.; Kobayashi, A.; Tokumoto, M.; Cassoux, P. Antiferromagnetic Organic Metal Exhibiting Superconducting Transition, κ-$(BETS)_2FeBr_4$ [Where BETS = Bis(ethylenedithio)tetraselenafulvalene]. *J. Am. Chem. Soc.* **1999**, *121*, 5581−5582.
(15) Coronado, E.; Galan-Mascaros, J. R.; Gomez-Garcia, C. J.; Laukhin, V. Coexistence of ferromagnetism and metallic conductivity in a molecule-based layered compound. *Nature* **2000**, *408*, 447.
(16) Petrovic, C.; Pagliuso, P. G.; Hundley, M. F.; Movshovich, R.; Sarrao, J. L.; Thompson, J. D.; Fisk, Z.; Monthoux, P. Heavy-fermion superconductivity in $CeCoIn_5$ at 2.3 K. *J. Phys.: Condens. Matter* **2001**, *13*, L337−L342.
(17) Bao, W.; Pagliuso, P. G.; Sarrao, J. L.; Thompson, J. D.; Fisk, Z.; Lynn, J. W.; Erwin, R. W. Incommensurate magnetic structure of $CeRhIn_5$. *Phys. Rev. B: Condens. Matter Mater. Phys.* **2000**, *62*, R14621.
(18) Petrovic, C.; Movshovich, R.; Jaime, M.; Pagliuso, P. G.; Hundley, M. F.; Sarrao, J. L.; Fisk, Z.; Thompson, J. D. A new heavy-fermion superconductor $CeIrIn_5$: A relative of the cuprates? *EPL* **2001**, *53*, 354.
(19) Stockert, O.; Arndt, J.; Faulhaber, E.; Geibel, C.; Jeevan, H. S.; Kirchner, S.; Loewenhaupt, M.; Schmalzl, K.; Schmidt, W.; Si, Q.; Steglich, F. Magnetically driven superconductivity in $CeCu_2Si_2$. *Nat. Phys.* **2010**, *7*, 119−124.
(20) Nanjundaswamy, K. S.; Vasanthacharya, N. Y.; Gopalakrishnan, J.; Rao, C. N. R. Convenient synthesis of the Chevrel phases metal molybdenum sulfide, $M_xMo_6S_8$ (M = copper, lead, lanthanum or gadolinium). *Inorg. Chem.* **1987**, *26*, 4286−4288.
(21) Machida, K.; Youngner, D. Superconductivity of ternary rare-earth compounds. *J. Low Temp. Phys.* **1979**, *35*, 449−463.
(22) Ishikawa, M.; Muller, J. Low temperature magnetization measurements on heavy rare earth molybdenum sulfides, $(RE)_{1.2}Mo_6S_8$. *Solid State Commun.* **1978**, *27*, 761−766.
(23) Shelton, R. N.; McCallum, R. W.; Adrian, H. Superconductivity in rare earth molybdenum selenides. *Phys. Lett. A* **1976**, *56*, 213−214.
(24) Cava, R. J.; Takagi, H.; Zandbergen, H. W.; Krajewski, J. J.; Peck, W. F., Jr; Siegrist, T.; Batlogg, B.; Van Dover, R. B.; Felder, R. J.; Mizuhashi, K.; et al. Superconductivity in the quaternary intermetallic compounds $LnNi_2B_2C$. *Nature* **1994**, *367*, 252.
(25) Pickett, W. E.; Singh, D. J. $LuNi_2B_2C$: A novel Ni-based strong-coupling superconductor. *Phys. Rev. Lett.* **1994**, *72*, 3702−3705.
(26) Lynn, J. W.; Skanthakumar, S.; Huang, Q.; Sinha, S. K.; Hossain, Z.; Gupta, L. C.; Nagarajan, R.; Godart, C. Magnetic order and crystal structure in the superconducting RNi_2B_2C materials. *Phys. Rev. B: Condens. Matter Mater. Phys.* **1997**, *55*, 6584−6598.
(27) Shulga, S. V.; Drechsler, S. L.; Fuchs, G.; Müller, K. H.; Winzer, K.; Heinecke, M.; Krug, K. Upper Critical Field Peculiarities of Superconducting YNi_2B_2C and $LuNi_2B_2C$. *Phys. Rev. Lett.* **1998**, *80*, 1730−1733.
(28) Eisaki, H.; Takagi, H.; Cava, R. J.; Batlogg, B.; Krajewski, J. J.; Peck, W. F., Jr; Mizuhashi, K.; Lee, J. O.; Uchida, S. Competition between magnetism and superconductivity in rare-earth nickel boride carbides. *Phys. Rev. B: Condens. Matter Mater. Phys.* **1994**, *50*, 647−650.
(29) Nakatsuji, S.; Kuga, K.; Machida, Y.; Tayama, T.; Sakakibara, T.; Karaki, Y.; Ishimoto, H.; Yonezawa, S.; Maeno, Y.; Pearson, E.; et al. Superconductivity and quantum criticality in the heavy-fermion system β-$YbAlB_4$. *Nat. Phys.* **2008**, *4*, 603−607.
(30) Fujioka, M.; Ishimaru, M.; Shibuya, T.; Kamihara, Y.; Tabata, C.; Amitsuka, H.; Miura, A.; Tanaka, M.; Takano, Y.; Kaiju, H.; et al. Discovery of the Pt-Based Superconductor $LaPt_5As$. *J. Am. Chem. Soc.* **2016**, *138*, 9927−9934.
(31) Rodríguez-Carvajal, J. Recent Advances in Magnetic Structure Determination by Neutron Powder Diffraction. *Phys. B* **1993**, *192*, 55−69.
(32) Sheldrick, G. M. Crystal Structure Refinement with SHELXL. *Acta Crystallogr., Sect. C: Struct. Chem.* **2015**, *71*, 3−8.
(33) *APEX2-Software Suite for Crystallographic Programs*; Bruker AXS Inc.: Madison, 2009.
(34) Blöchl, P. E. Projector augmented-wave method. *Phys. Rev. B: Condens. Matter Mater. Phys.* **1994**, *50*, 17953.

https://dx.doi.org/10.1021/acscentsci.0c00691
ACS Cent. Sci. 2020, 6, 2023−2030

(35) Kresse, G.; Joubert, D. From ultrasoft pseudopotentials to the projector augmented-wave method. *Phys. Rev. B: Condens. Matter Mater. Phys.* **1999**, *59*, 1758.
(36) Hafner, J. Ab-Initio Simulations of Materials Using VASP: Density-Functional Theory and Beyond. *J. Comput. Chem.* **2008**, *29*, 2044−2078.
(37) Perdew, J. P.; Burke, K.; Ernzerhof, M. Generalized Gradient Approximation Made Simple. *Phys. Rev. Lett.* **1996**, *77*, 3865−3868.
(38) Dahl, J. P.; Avery, J. *Local Density Approximations in Quantum Chemistry and Solid State Physics*; Springer Science & Business Media, 2013.

https://dx.doi.org/10.1021/acscentsci.0c00691
ACS Cent. Sci. 2020, 6, 2023−2030